A Thermally Insulating Cryogenic Medium-Frequency Transformer for Use in a Cryogenic GaN Dual Active Bridge

1st Frank, S.R.
Institute of Electrical Engineering (ETI)
Karlsruhe Institute of Technology (KIT),
Karlsruhe, Germany
s.frank@kit.edu

2nd Ehrlich, L.
Institute of Electrical Engineering (ETI)
Karlsruhe Institute of Technology (KIT),
Karlsruhe, Germany
lucas.ehrlich@kit.edu

3th Schwendemann, R.
Institute of Electrical Engineering (ETI)
Karlsruhe Institute of Technology (KIT),
Karlsruhe, Germany
ruediger.schwendemann@kit.edu

4th Hiller, M.
Institute of Electrical Engineering (ETI)
Karlsruhe Institute of Technology (KIT),
Karlsruhe, Germany
marc.hiller@kit.edu

***Abstract*—A key challenge in cryogenic applications is managing heat input from the warmer environment. This paper presents a novel Medium-Frequency Transformer (MFT) concept designed for converter integration as a thermal insulator at cryogenic temperatures. First, the basic idea of the thermally insulating transformer is outlined, followed by electromagnetic dimensioning and thermal design considerations. Detailed simulations illustrate the effects of critical design parameters on thermal and electromagnetic performance. Based on these insights, a prototype MFT is developed and integrated into a 20 kW/100 kHz Dual Active Bridge (DAB) converter topology. Measurement results validate the functionality of the developed MFT in conjunction with the DAB, demonstrating its potential for efficient thermal management in cryogenic environments.**

***Index Terms*—Wide-Bandgap, GaN, Cryogenic, Dual Active Bridge (DAB), Measurements**

I. Motivation

The increasing number of High Temperature Superconductor (HTS) applications such as power supply lines, superconducting wind generators, and electric aircraft opens up a wide field for cryogenic power electronics [1]–[7]. All applications have in common a cryogenic system part, consisting of the HTS, and one or more interface(s) to the warmer environment which are necessary to exchange electrical power. However, those interfaces introduce heat input, which in turn reduces the efficiency of the system due to the higher demand for cryogenic cooling power. Typically, the interfaces are realized with copper current leads to ensure low electrical losses. This paper proposes a power electronics converter instead, which transmits the electrical power inductively instead of conductively. The selected DAB circuit and the implemented back-to-back test bench, consisting of two DAB converters, are shown Fig. 1, Table I summarizes all relevant parameters.

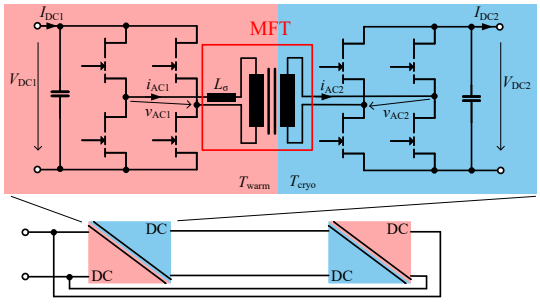

Fig. 1: Cryogenic DABs with GaN-HEMTs

One key component is the MFT that insulates both domains, galvanically and thermally. While low-frequency transformers with one or more cryogenic (HTS) winding(s) are already reported in literature [8]–[10], there are very few concepts for higher frequencies. In [11], a 1.5 kW/200 kHz transformer for cryogenic and vacuum operating conditions is presented. However, in this concept the complete transformer operates at cryogenic temperature and no thermal insulation is provided. The only reported MFT with explicit thermal insulation is described in [12] and operates with 4 kHz. Higher frequencies allow size reduction and higher power density, but pose some challenges in the transformer design.

TABLE I: Design Parameters DAB

Semiconductors	*GaN Systems GS66516T*
Nominal power P_N	20 kW
DC link voltage $V_{DC1} = V_{DC2}$	400 V
Switching frequency f_{sw}	100 kHz
Transformer leakage inductance L_σ	$< 10\,\mu H$
Transformer turns ratio a	1 : 1

This work explicitly investigates the thermal insulation of the cryogenic transformer operating at a high switching frequency of $f_{\mathrm{sw}} = 100\,\mathrm{kHz}$ with Gallium Nitride (GaN)-High Electron Mobility Transistors (HEMTs).

II. Design Challenges for a Medium Frequency Cryogenic Thermally Insulating Transformer

According to [13], the power transferred by a DAB with single phase shift modulation

$$P = \frac{V_{\mathrm{DC1}} \cdot V_{\mathrm{DC2}} \cdot \varphi}{2 \cdot \pi \cdot L_{\sigma} \cdot f_{\mathrm{sw}}} \cdot \left(1 - \frac{|\,\varphi\,|}{\pi}\right), \tag{1}$$

is calculated with the DC voltages V_{DC1} and V_{DC2}, the switching frequency f_{sw}, the switching angle φ between both AC voltages v_{AC1} and v_{AC2} and the leakage inductance of the transformer L_{σ}. To reach a high maximum transferable power at high switching frequencies, the leakage inductance has to be small. This can be realized by arranging the primary and secondary winding close to each other. However, for good thermal insulation, both windings have to be separated from each other. These conflicting optimization criteria are examined in more detail in section IV.

Another challenge is the cooling of the cryogenic winding. In this paper, three approaches are considered, that are summarized in Fig. 2. The first approach (a) which is used in [9] for instance, is to put the whole cryogenic winding into a hermetic cryostat and to use a liquid coolant such as Liquid Nitrogen ($\mathrm{LN_2}$) in direct contact with the winding. This ensures a low thermal resistance between winding and coolant. Nevertheless, it comes with the downside of the challenging manufacturing of the cryostat, especially when the transformer is operated in vacuum and a hermetic feed-through of the windings litz wires is necessary. Furthermore, the cryostat introduces an additional space between the primary and secondary winding, which increases L_{σ}.

The second approach (b) is to only actively cool both ends of the winding, for instance by using cryogenic cold heads. Therefore no cryostat is required inside the transformer and both windings can be put closer together. For this type of approach, it is essential to have a good thermal connection between the winding and the cold heads. Consequently, the required copper cross-sectional area of the litz wires is greater than that of the other two approaches.

In the following sections, a prototype based on a third approach (c), realized with a cryogenic ceramic winding holder, is presented. The ceramic ensures an effective conductive cooling of the complete winding. In comparison to the first approach, the distance between primary and secondary winding is reduced, ensuring a smaller leakage inductance. Compared to the second approach, the increased cooling surface allows for a reduction in the copper cross-section of the windings.

III. Electromagnetic Design

The magnetic characteristics of various core materials at cryogenic temperatures are reported in literature [14]–[16]. The comparison of the parameters in [11] shows that for all

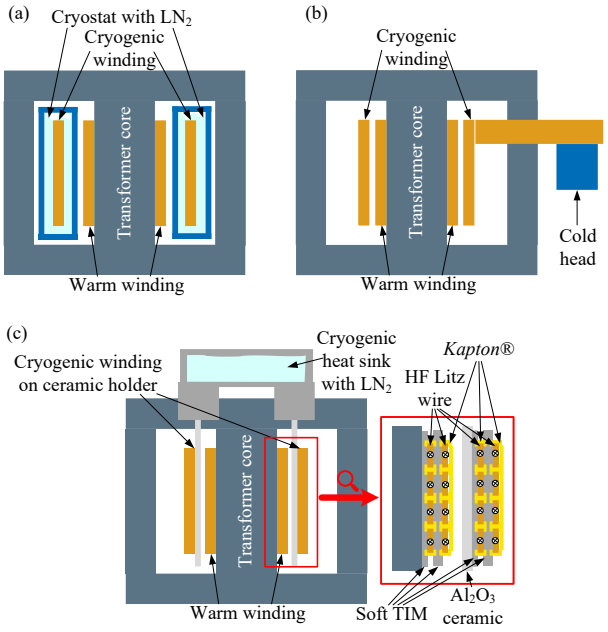

Fig. 2: Cooling approaches for the cryogenic winding of the MFT. (a) Immersed in $\mathrm{LN_2}$, (b) Cooling applied exclusively to the winding ends, (c) Ceramic winding holder

investigated materials the core losses increase significantly at cryogenic temperature of 77 K. For this reason, in this work the transformer core is kept warm. Due to the availability of a wide range of geometries, low costs and moderate core losses, the *BFM9* ferrite material [17] from *Blinzinger* is used.

The windings are realized with High Frequency (HF) litz wires to mitigate the skin effect. With the transformer's fundamental frequency f_{sw} of 100 kHz and the material parameters of copper the skin depth $\delta \approx 209\,\mu\mathrm{m}$ at Room Temperature (RT) is calculated. It should be noted that at cryogenic temperatures, the skin depth is reduced due to the reduced specific resistance of copper. The selection of $71\,\mu\mathrm{m}$ strand diameter ensures an efficient utilization of the conductor's cross-sectional area. The selected litz wire *RUPALIT Flecht Profil V155* consists of 1998 strands, offering a total conductor area of $7.91\,\mathrm{mm}^2$. This results in a theoretical DC resistance of $2.18\,\mathrm{m\Omega\,m^{-1}}$ at 300 K. At 77 K the resistance decreases by a factor of $\approx$ 5..8.5, depending on the materials purity [18]. Measurements with a sample of the selected wire show $2.46\,\mathrm{m\Omega\,m^{-1}}$ at 300 K and $0.31\,\mathrm{m\Omega\,m^{-1}}$ at 77 K, which corresponds to a factor of 7.9.

To implement the two separated cooling systems as described in the following section and to ensure a small leakage inductance at the same time, two E-cores are selected with both windings wrapped around the round center core as seen in Fig. 3. Several 3D-Finite Element Method (FEM) simulations are carried out using *Ansys Maxwell* to determine the influence of geometric parameters on leakage inductance L_{σ}, core losses P_{core} and copper losses P_{co}. Beside the

distance between both windings d_{iso}, which strongly depends on the cooling design and primarily affects L_σ, the diameter of the core d_{core} and the number of turns n per winding influence all three quantities. To achieve a good distribution of core and copper losses, while maintaining L_σ of less than $10\,\mu\mathrm{H}$, $d_{\mathrm{core}} = 50\,\mathrm{mm}$ and $n = 11$ are chosen, resulting in $P_{\mathrm{core}} \approx 30\,\mathrm{W}$ (simulated value) and $P_{\mathrm{co}} \approx 31\,\mathrm{W}$ (calculated value) at the nominal power $P_{\mathrm{N}} = 20\,\mathrm{kW}$. Note that the copper losses for both windings $P_{\mathrm{co}} = P_{\mathrm{co,warm}} + P_{\mathrm{co,cryo}}$ are calculated for the worst-case scenario, in which both windings operate at 300 K. During cryogenic operation the losses of the cryogenic winding are reduced by a factor of approximately 8, resulting in $P_{\mathrm{co,warm}} \approx 13\,\mathrm{W}$ and $P_{\mathrm{co,cryo}} \approx 18\,\mathrm{W}/8 = 2.25\,\mathrm{W}$. To ensure enough space for the cooling in the winding window, two *ETD160/73/50* cores with the dimensions shown in Fig. 4 are selected. To further decrease L_σ, both windings are designed as two layer windings, which offers the advantage that the start and end of each winding are at the same point.

IV. Thermal Design

The transformer is cooled using two separated cooling systems. As shown in Fig. 3, the core and the warm winding, which is directly wound around the core, are water-cooled, while for the cryogenic winding $\mathrm{LN_2}$ is used as coolant. The whole setup is operated in vacuum to prevent icing and to ensure the thermal insulation of the cryogenic part. For this reason, the entire heat loss must be dissipated via heat radiation or heat conduction. To achieve this, the ferrite core is embedded in an aluminum water heat sink. At all contact areas a soft, silicone-based Thermal Interface Material (TIM) is used to ensure a proper thermal connection between the warm winding, the core and the heat sink. For both windings, a rectangular shaped litz wire is used, which provides a large contact area. The winding structure is shown in detail in Fig. 2(c).

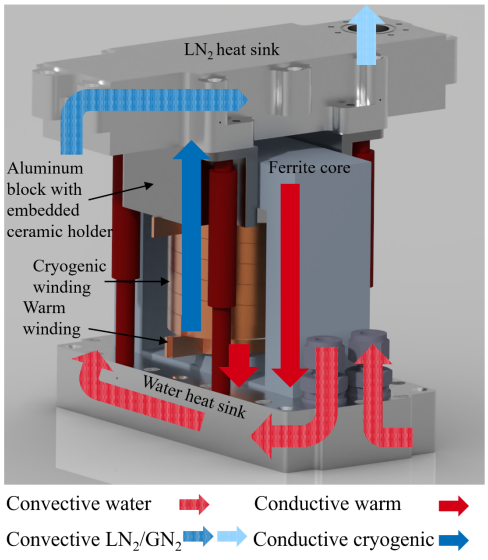

Fig. 3: Cooling circuits

For the cryogenic winding, a ceramic winding holder is used. Table II provides an overview of the materials investigated and their key properties relevant to their use in the transformer. These include the thermal conductivities at RT $\lambda_{300\mathrm{K}}$ and if available at cryogenic temperature $\lambda_{77\mathrm{K}}$, the electrical conductivity and the mechanical processability.

TABLE II: Materials Cryogenic Winding Holder

Material	$\lambda_{300\mathrm{K}}$ in W/Km	$\lambda_{77\mathrm{K}}$ in W/Km	Electrical conduct.	Mech. proc.	Costs
AlN [19]	≈ 240	≈ 600	isolator	-	€€€
Al_2O_3 [20]–[22]	≈ 25	≈ 90	isolator	+	€
SiSiC [23]	≈ 160	?	semicon.	+	€€
MACOR [24]	≈ 1.5	?	isolator	++	€
Shapal Hi-M Soft [25]	≈ 90	?	isolator	++	€€

Silicon Infiltrated Silicon Carbide (SiSiC), Aluminum Nitride (AlN) and *Shapal Hi-M Soft* offer the highest thermal conductivity. However, the additively manufactured SiSiC ceramic supplied by *CeramTec* exhibits an electrical conductivity of approximately $8800\,\mathrm{S/m}$, which is sufficiently high to induce significant eddy current losses. Aluminum Nitride (AlN) and the AlN-Boron Nitride (BN) composite ceramic *Shapal Hi-M Soft* are good electrical isolators but generally more costly compared to Aluminum Oxide ($\mathrm{Al_2O_3}$). For these reasons, $\mathrm{Al_2O_3}$ is selected for the first prototype. It features a relatively high thermal conductivity of $\lambda_{\mathrm{Al2O3}} \approx 25\,\mathrm{W\,K^{-1}\,m^{-1}}$, which increases even further at cryogenic temperatures [20], [21], a good temperature stability and mechanical processability as well as moderate costs.

To enhance the heat dissipation from the windings and simultaneously reduce the manufacturing costs, only the section of the holder located between the two windings is fabricated from $\mathrm{Al_2O_3}$ ceramic to prevent eddy currents. Outside the area of high magnetic fields, the ceramic is embedded in an aluminum block, which is mounted to an aluminum heat sink, containing the $\mathrm{LN_2}$. High thermal conductivity and low thermal contact resistances are essential, since all ohmic losses should be dissipated purely conductively.

Several thermal FEM simulations are performed with *COMSOL Multiphysics* to optimize the geometry of the winding holder and to investigate the interface between the cryogenic and the warm transformer parts. As described in the sections before, the distance between the warm and the cryogenic winding d_{iso} must be kept as low as possible. A minimum holder thickness of $3\,\mathrm{mm}$ is required to maintain mechanical integrity and to comply with the manufacturing process constraints of the $\mathrm{Al_2O_3}$ material. In addition, an extra clearance of $2\,\mathrm{mm}$ is allocated to account for the vacuum insulation layer and a potential thermal shield, yielding a total insulation thickness of $d_{\mathrm{iso}} = 5\,\mathrm{mm}$.

In Fig. 4 two exemplary temperature distributions for the implemented geometry in thermal steady state are depicted. The simulation results were obtained by using a multiphysics model incorporating solid-state heat conduction and surface-to-surface radiative heat exchange. The ambient temperature is set to $T_{\mathrm{amb}} = 293\,\mathrm{K}$ and the losses are defined as evenly

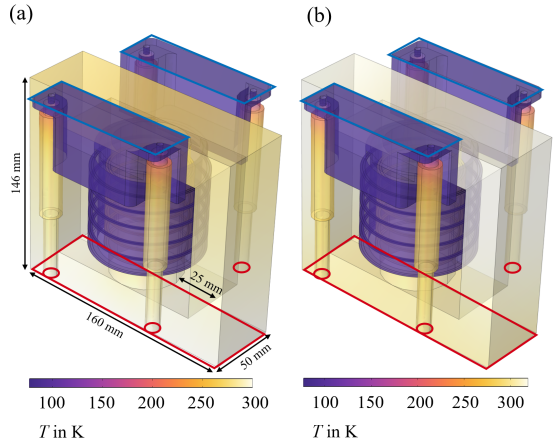

Fig. 4: Thermal simulation results. (a) No transmitted power, (b) Nominal power with corresponding losses (see section III)

distributed volume losses across the turns of both windings and the core. Due to symmetry considerations, only 10 turns per winding are considered in the analysis. In the actual transformer, the 11th turn corresponds to the turn between the two winding layers. Each turn is idealized as a solid copper cylinder. A $100\,\mu\mathrm{m}$ *Kapton* insulation layer surrounding the windings is included in the model, whereas the TIM and all thermal contact resistances are neglected. The material parameters are taken from the *COMSOL* library. For the ceramic winding holder, a solid polycrystalline Al_2O_3 material is assumed, with its thermal conductivity reduced by a factor of 0.6 to account for the lower conductivity of the 96% Al_2O_3 ceramic used in the real setup [22].

Areas marked in blue are held at $77\,\mathrm{K}$, representing the contact areas to the cryogenic LN_2 heat sink. Areas marked in red are held at $300\,\mathrm{K}$, describing the contact areas to the water heat sink. Figure 4(a) illustrates the temperature distribution in the idle state with no power losses, while Fig. 4(b) shows the corresponding distribution including the losses $P_{\mathrm{core}} = 30\,\mathrm{W}$, $P_{\mathrm{co,warm}} = 13\,\mathrm{W}$ and $P_{\mathrm{co,cryo}} = 2.25\,\mathrm{W}$ at nominal power $P_{\mathrm{N}} = 20\,\mathrm{kW}$.

The thermal separation of the cryogenic and the warm parts is clearly visible. Under idle conditions, the cryogenic section reaches a maximum temperature of $83.3\,\mathrm{K}$, whereas the warm section exhibits a minimum temperature of $259.3\,\mathrm{K}$, corresponding to a temperature gradient of $\Delta T_{\mathrm{sim,idle}} = 176\,\mathrm{K}$ across the transformer. When the losses at nominal operation power are considered, the temperatures in the core and warm winding increase, while those in the cryogenic components remain nearly constant. With a maximum temperature of $84.9\,\mathrm{K}$ in the cryogenic parts and a minimum temperature of $288.5\,\mathrm{K}$ in the warm parts this results in a temperature gradient $\Delta T_{\mathrm{sim,N}} = 203.6\,\mathrm{K}$.

One of the key objectives of the development is to minimize the heat input into the cryogenic system parts. Due to the vacuum operation and the usage of only thin Polychlorotrifluoroethylene (PCTFE) support pillars as depicted in Fig. 5 for the LN_2 heat sink, the only relevant remaining heat transfer into the cryogenic winding is via heat radiation. The radiated net heat flow

$$\dot{Q}_{\mathrm{rad}} = \frac{\sigma \cdot A_{\mathrm{warm}} \cdot (T_{\mathrm{warm}}^4 - T_{\mathrm{cryo}}^4)}{\frac{1}{\epsilon_{\mathrm{warm}}} + \frac{A_{\mathrm{warm}}}{A_{\mathrm{cryo}}} \cdot (\frac{1}{\epsilon_{\mathrm{cryo}}} - 1)}, \tag{2}$$

is calculated based on the Stefan-Boltzmann law with σ being the Stefan-Boltzmann constant. Assuming an emissivity ϵ_{warm} of 0.84 as worst-case assumption from the given values in [26], [27] for the outer *Kapton*® layer (see Fig. 2(c)), ϵ_{cryo} of 0.75 for the cryogenic ceramic [28], the radiation surfaces $A_{\mathrm{warm}} = 2\pi \cdot 30.2\,\mathrm{mm} \cdot 72\,\mathrm{mm} \approx 137\,\mathrm{cm}^2$ and $A_{\mathrm{cryo}} = 2\pi \cdot 32.5\,\mathrm{mm} \cdot 72\,\mathrm{mm} \approx 147\,\mathrm{cm}^2$ as well as the temperatures $T_{\mathrm{warm}} = 320\,\mathrm{K}$ and $T_{\mathrm{cryo}} = 77\,\mathrm{K}$ leads to $\dot{Q}_{\mathrm{rad}} \approx 5.4\,\mathrm{W}$. $T_{\mathrm{warm}} = 320\,\mathrm{K}$ corresponds to the maximum temperature at nominal power, whereas $T_{\mathrm{cryo}} = 77\,\mathrm{K}$ was chosen as worst-case assumption.

To reduce this heat flow, a thermal shield could be used. Due to its position between the two windings, any metallic shield will inevitably experience induced eddy currents. To keep the currents to a minimum, the thickness of the metallic layers has to be in the nanometer range and large metallic areas have to be avoided. A possible solution could be a segmented superinsulation as *COOLCAT 2 NI* from *Beyond Gravity* [29], promising a heat flow $P_{\mathrm{rad}} < 0.1\,\mathrm{W}$ with the specified heat flux of $4.6\,\mathrm{W\,m^{-2}}$. The use of such a superinsulation is the subject of future research with the proposed prototype.

V. Measurements with the Prototype

Based on the dimensioning in the previous sections, the prototype shown in Fig. 5 is built. Figure 5(a) illustrates the cryogenic winding during manufacturing, with the inner layer already wound onto the ceramic holder and the TIM visible. In Fig. 5(b) the completed transformer with exposed thermal contact areas to the LN_2 heat sink is depicted.

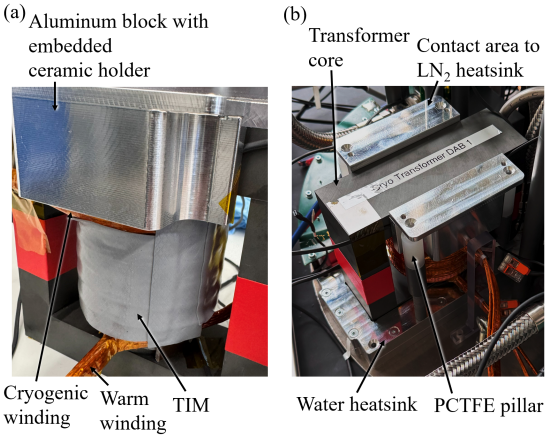

Fig. 5: MFT prototype. (a) During manufacturing, (b) Built into the test setup

To investigate the electromagnetic behavior, the leakage inductance L_σ over frequency is measured by using an *E4990A* impedance analyzer from *Keysight*. A second measurement

performed with the *DPG10* power choke tester from *ed-k* determines the inductance as a function of current to investigate the saturation behavior.

Figure 6 depicts the frequency dependency of the leakage inductance L_σ. In the 100 kHz range, its value stays constant at approximately 4.4 µH, the first resonance occurs at around 6 MHz. The current dependency of L_σ is shown in Fig. 7. There is no saturation, L_σ stays constant at around 4.6 µH over the whole investigated current range up to 150 A, which corresponds very well with the impedance analyzer measurements and fulfills the design goal of $L_\sigma < 10\,\mu\text{H}$.

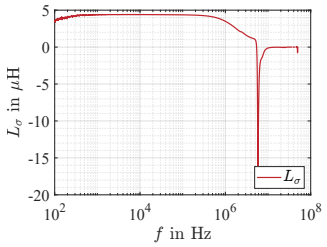

Fig. 6: L_σ over frequency

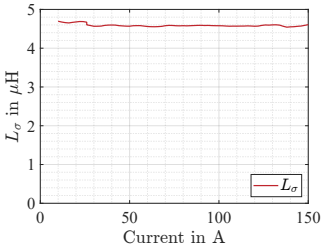

Fig. 7: L_σ over current

Subsequently, the thermal performance of the transformer is analyzed. To monitor the temperatures during operation and for investigation of the cryogenic-to-warm interface, eleven PT1000 temperature sensors are placed in the windings, on the holders, the core, and the heat-sinks as depicted in Fig. 8.

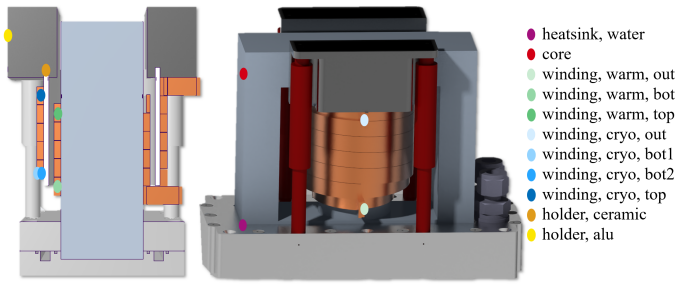

Fig. 8: Temperature sensors position

Prior to cooling with LN_2, the transformer is placed in a stainless-steel container that is evacuated to minimize residual gas content, prevent icing and increase the thermal insulation. The temperatures recorded during the cooling are depicted in Fig. 9, the colors correspond to the temperature sensor definition given in Fig. 8. In this measurement condition, no electrical power is transferred through the transformer, and thus no electrical losses occur.

The thermal steady state for the cryogenic parts is reached after approximately 1 h. The temperatures measured at that time are presented in Table III. For comparison, the corresponding simulation results without any electrical losses are listed as well. The higher temperatures of the cryogenic parts in the measurement are likely a result of the thermal contact resistances not being accounted for in the simulation. Excluding the light-blue sensor "winding, cryo, out", which

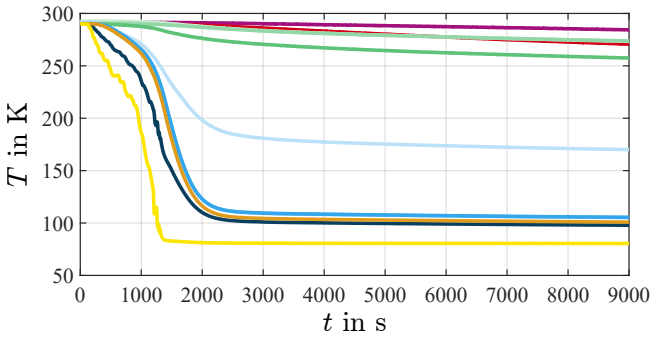

Fig. 9: Measured temperature curves of the MFT during cooling

is located outside the transformer in the lead-in litz wire, a thermal gradient $\Delta T_{\text{meas,idle}}$ of approximately 159.7 K can be observed.

It is evident that the temperatures of the warmer transformer components have not yet reached thermal steady state, which can be attributed to the gradual cooling of the stainless-steel enclosure resulting from imperfect thermal insulation.

TABLE III: Temperatures of the MFT

Location	Temperature Simulation	Temperature Measurement
Core	300 K	284.3 K
Winding, warm, bot	265.8 K	281.7 K
Winding, warm, top	259.4 K	268.4 K
Winding, cryo, bot1/2	83.2 K	108.7 K
Winding, cryo, top	80.7 K	100.4 K
Holder, alu	77.1 K	80.7 K

To verify the proper function of the DAB and to characterize the MFT under operating conditions, a back-to-back test bench, consisting of two identical DABs, is used. The whole test bench is illustrated in Fig. 10. The depicted stainless-steel container houses both DAB converters, connected as illustrated in Fig. 1. During operation, the two DABs are enclosed in vacuum, with one operating under voltage control and the other under current control.

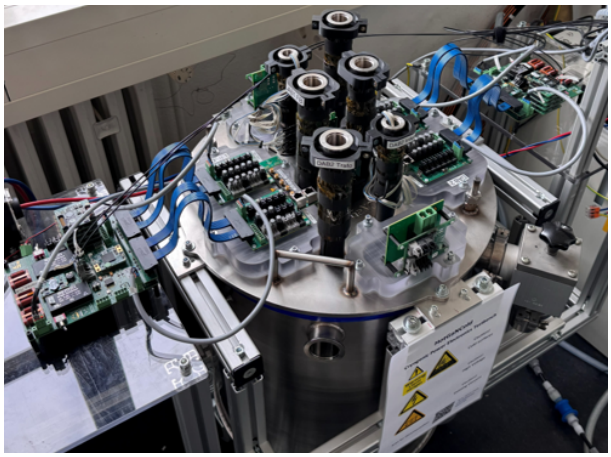

Fig. 10: Cryogenic DAB test bench

This paper presents the first measurements with reduced voltages $V_{\mathrm{DC1}} = V_{\mathrm{DC2}} = 40\,\mathrm{V}$ and currents $I_{\mathrm{DC1}} = I_{\mathrm{DC2}} = 5\,\mathrm{A}$. Both values are reduced by a factor of ten to maintain the same voltage-to-current ratio as in the nominal operating point. The current of the cryogenic winding i_{AC2} is measured using a *CWTUM/1/R* Rogowski coil with 30 MHz bandwidth, for the voltage v_{AC2} an optically isolated *MicSig MOIP02P* probe with 200 MHz bandwidth and a $50:1$ probe tip is used. The signals are sampled with $10\,\mathrm{GS/s}$ using a *LeCroy MDA 8058HD* oscilloscope. Figure 11 illustrates the waveforms. The effective leakage inductance can be calculated from the current gradients shown as $L_\sigma \approx 4.7\,\mu\mathrm{H}$.

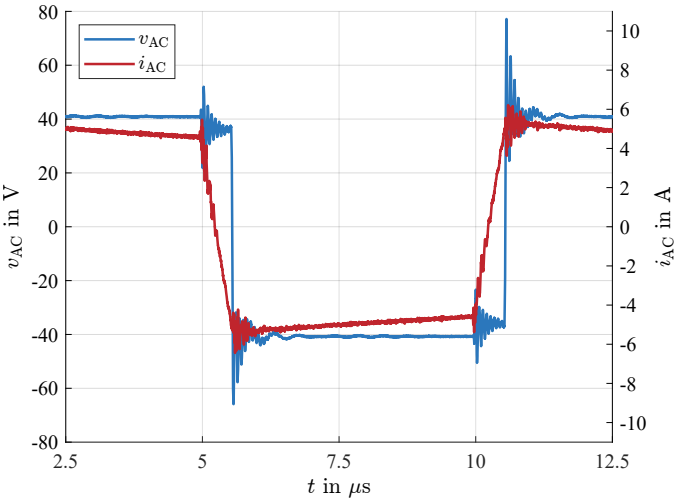

Fig. 11: Waveforms cryogenic MFT in DAB operation

VI. Conclusion and Future Work

This paper presents an innovative, thermally insulating MFT with one cryogenic winding for operation at 100 kHz, 400 V and 50 A. It is based on a novel cooling concept, which incorporates two separate cooling circuits, one water-based and one utilizing $\mathrm{LN_2}$. This concept allows a thermal separation of the cryogenic winding, reducing heat input and thus the required cooling capacity. At the same time the leakage inductance, which limits the transferable power in DAB operation is kept below 5 µH, enabling efficient transmission of high power.

The proper electromagnetic function is demonstrated with a reduced voltage of 40 V and a current of 5 A in a back-to-back DAB test bench with one winding operating at cryogenic temperatures below 110 K. The thermal insulation between the cryogenic and the warm transformer parts was demonstrated by analyzing the temperature distribution inside the transformer. A temperature gradient of approximately 159.7 K was measured. The presented prototype offers a unique possibility to investigate the cryogenic-to-warm interface, which is essential for all HTS applications. Furthermore, it provides a versatile platform for research on power electronics at this thermal interface.

Acknowledgment

This work was carried out within the hydrogen flagship project TransHyDE and was funded by the Federal Ministry of Education and Research under the funding grant number 03HY204A. The responsibility for the content of this publication lies with the authors.

References

[1] S. Lengsfeld, J. Grundmann, M. Oomen, C. Vargas-Llanos, B. Ponick, and M. Jung, "Comparing Armature Windings for a 10 MW Fully Superconducting Synchronous Wind Turbine Generator," in *2022 12th International Conference on Power, Energy and Electrical Engineering (CPEEE)*. Shiga, Japan: IEEE, Feb. 2022, pp. 49–53. [Online]. Available: https://ieeexplore.ieee.org/document/9738712/

[2] S. Miura, M. Iwakuma, and T. Izumi, "Lightweight Design of Tens-MW Fully-Superconducting Wind Turbine Generators With High-Performance $\mathrm{REBa_2\,Cu_3\,O_y}$ Wires," *IEEE Transactions on Applied Superconductivity*, vol. 30, no. 4, pp. 1–6, Jun. 2020. [Online]. Available: https://ieeexplore.ieee.org/document/9028170/

[3] H.-W. Cho, T.-K. Bang, J.-I. Lee, K.-H. Shin, H.-S. Lee, J.-S. Hur, and K. S. Haran, "Design and Preliminary Experiments of a Rotating Armature Partial Superconducting Air-Core Generator," *IEEE Transactions on Applied Superconductivity*, vol. 32, no. 6, pp. 1–5, Sep. 2022. [Online]. Available: https://ieeexplore.ieee.org/document/9787704/

[4] P. Alvarez, M. Satrústegui, S. G. Scheifler, J. Bastarrarena, L. G. López, and M. Martinez-Iturralde, "Design of a HTS 2 MW Electric Motor for Single-Aisle Regional Aircraft," *IEEE Access*, vol. 11, pp. 144 325–144 336, 2023. [Online]. Available: https://ieeexplore.ieee.org/document/10363191/

[5] Y. Wang, L. Zhou, Q. Yuan, and X. Song, "Feasibility Study of High Temperature Superconducting Machines for Electric Aircraft," in *2024 IEEE 7th International Electrical and Energy Conference (CIEEC)*. Harbin, China: IEEE, May 2024, pp. 1082–1087. [Online]. Available: https://ieeexplore.ieee.org/document/10583838/

[6] M. Stemmle, F. Merschel, M. Noe, L. Hofmann, and A. Hobl, "Superconducting MV cables to replace HV cables in urban area distribution grids," in *PES T&D 2012*. Orlando, FL, USA: IEEE, May 2012, pp. 1–5. [Online]. Available: http://ieeexplore.ieee.org/document/6281443/

[7] A. Allais, J.-M. Saugrain, B. West, N. Lallouet, H. Caron, D. Ferandelle, L. Terrien, G. Bouvier, G. Hajiri, K. Berger, and L. Quéval, "SuperRail–World-First HTS Cable to be Installed on a Railway Network in France," *IEEE Transactions on Applied Superconductivity*, vol. 34, no. 3, pp. 1–7, May 2024. [Online]. Available: https://ieeexplore.ieee.org/document/10415193/

[8] A. Formisano, F. Marignetti, R. Martone, G. Masullo, A. Matrone, R. Quarantiello, and M. Scarano, "Performance Evaluation for a HTS Transformer," *IEEE Transactions on Applied Superconductivity*, vol. 16, no. 2, pp. 1501–1504, Jun. 2006. [Online]. Available: http://ieeexplore.ieee.org/document/1643139/

[9] S. Hellmann, "Research and Technology Development on Superconducting Current Limiting Transformers," Ph.D. dissertation, KIT, 2018.

[10] N. Glasson, M. Staines, N. Allpress, M. Pannu, J. Tanchon, E. Pardo, R. Badcock, and R. Buckley, "Test Results and Conclusions From a 1 MVA Superconducting Transformer Featuring 2G HTS Roebel Cable," *IEEE Transactions on Applied Superconductivity*, vol. 27, no. 4, pp. 1–5, Jun. 2017. [Online]. Available: http://ieeexplore.ieee.org/document/7782407/

[11] Z. Zhang, N. Bharmal, Y. Zhang, J. Fan, Y. Yao, R. Guenther, P. Fu, and J. Wang, "A 200-kHz/1.5-kW Multi-winding Transformer for Lunar Surface Power Applications," in *2023 IEEE Energy Conversion Congress and Exposition (ECCE)*. Nashville, TN, USA: IEEE, Oct. 2023, pp. 6080–6086. [Online]. Available: https://ieeexplore.ieee.org/document/10362279/

[12] P. C. Saha, Y. Shi, M. Steurer, P. Cheetham, C. Kim, S. Pamidi, J. Goldman, B. German, Z. Jin, L. Graber, and C. Park, "CLEAN: Cryogenic Link for Electric Aircraft Propulsion," *IEEE Transactions on Applied Superconductivity*, vol. 33, no. 5, pp. 1–6, Aug. 2023. [Online]. Available: https://ieeexplore.ieee.org/document/10034797/

[13] R. De Doncker, D. Divan, and M. Kheraluwala, "A three-phase soft-switched high-power-density DC/DC converter for high-power applications," *IEEE Transactions on Industry Applications*, vol. 27, no. 1, pp. 63–73, Feb. 1991. [Online]. Available: http://ieeexplore.ieee.org/document/67533/

[14] R. Chen, Z. Dong, Z. Zhang, H. Gui, J. Niu, R. Ren, F. Wang, L. M. Tolbert, B. J. Blalock, D. J. Costinett, and B. B. Choi, "Core Characterization and Inductor Design Investigation at Low Temperature," in *2018 IEEE Energy Conversion Congress and Exposition (ECCE)*. Portland, OR, USA: IEEE, Sep. 2018, pp. 4218–4225. [Online]. Available: https://ieeexplore.ieee.org/document/8557779/

[15] A. Wadsworth, S. McKeown, D. J. Thrimawithana, M. G. Pearce, L. Zhao, Z. Li, and M. Neuburger, "Cryogenic Evaluation of Nanocrystalline Cores Using Partial Cancellation," in *2022 Wireless Power Week (WPW)*. Bordeaux, France: IEEE, Jul. 2022, pp. 680–684. [Online]. Available: https://ieeexplore.ieee.org/document/9853904/

[16] S. Yin, M. Mehrabankhomartash, A. J. Cruz, L. Graber, M. Saeedifard, S. Evans, F. Kapaun, I. Revel, G. Steiner, L. Ybanez, and C. Park, "Characterization of Inductor Magnetic Cores for Cryogenic Applications," in *2021 IEEE Energy Conversion Congress and Exposition (ECCE)*. Vancouver, BC, Canada: IEEE, Oct. 2021, pp. 5327–5333. [Online]. Available: https://ieeexplore.ieee.org/document/9595353/

[17] B. E. Components, "Blinzinger_ferritkern_e130-64-40." [Online]. Available: https://www.blinzinger-elektronik.de/ferrite/

[18] S. Calatroni, "Materials & Properties: Thermal & Electrical Characteristics," 2020, version Number: 1. [Online]. Available: https://arxiv.org/abs/2006.02842

[19] R. L. Xu, M. Muñoz Rojo, S. M. Islam, A. Sood, B. Vareskic, A. Katre, N. Mingo, K. E. Goodson, H. G. Xing, D. Jena, and E. Pop, "Thermal conductivity of crystalline AlN and the influence of atomic-scale defects," *Journal of Applied Physics*, vol. 126, no. 18, p. 185105, Nov. 2019. [Online]. Available: https://pubs.aip.org/jap/article/126/18/185105/156345/Thermal-conductivity-of-crystalline-AlN-and-the

[20] T. Nemoto, S. Sasaki, and Y. Hakuraku, "Thermal Conductivity of Alumina and Silicon Carbide Ceramics at Low Temperatures," Mar. 1985.

[21] N. Simon, "Cryogenic Properties of Inorganic Insulation Materials for ITER Magnets: A Review," Tech. Rep. NISTIR-5030, 761710, Dec. 1994. [Online]. Available: http://www.osti.gov/servlets/purl/761710-u8kdDW/webviewable/

[22] bce special ceramics, "Material Data Sheet Alumina A-960." [Online]. Available: https://www.bce-special-ceramics.com/wp-content/uploads/2016/11/A_960.pdf

[23] ceramtec, "Additive manufacturing without compromise – ROCAR® 3D Silicon Carbide." [Online]. Available: https://www.ceramtec-group.com/fileadmin/user_upload/Corporate/11_Downloads/15_Various_Industrial_Applications/Datasheet_CeramTec_3D-Printing_SiSC.pdf

[24] C. Incorporated, "MARCOR-Technical-Datasheet." [Online]. Available: https://psec.uchicago.edu/ceramics/MACOR%20Data%20Sheet.pdf

[25] precision ceramics, "Shapal-Technical-Data-Sheet." [Online]. Available: https://precision-ceramics.com/wp-content/uploads/Shapal-Technical-Data-Sheet-de.pdf

[26] T. Xiao, X. Fan, D. Fan, and Q. Li, "High thermal conductivity and low absorptivity/ emissivity properties of transparent fluorinated polyimide films," *Polymer Bulletin*, vol. 74, no. 11, pp. 4561–4575, Nov. 2017. [Online]. Available: http://link.springer.com/10.1007/s00289-017-1974-6

[27] T. Okada, R. Ishige, and S. Ando, "Analysis of Thermal Radiation Properties of Polyimide and Polymeric Materials Based on ATR-IR spectroscopy," *Journal of Photopolymer Science and Technology*, vol. 29, no. 2, pp. 251–254, 2016. [Online]. Available: https://www.jstage.jst.go.jp/article/photopolymer/29/2/29_251/_article

[28] W. Zhao, Z. Sun, and Z. T. Alwahabi, "Emissivity and absorption function measurements of Al2O3 and SiC particles at elevated temperature for the utilization in concentrated solar receivers," *Solar Energy*, vol. 207, pp. 183–191, Sep. 2020. [Online]. Available: https://linkinghub.elsevier.com/retrieve/pii/S0038092X20306939

[29] B. Gravity, "Beyond-Gravity-Cryogenic-Insulation-Products," Jan. 2023. [Online]. Available: beyondgravity.com